A new development for the WBW model at elevated pressure levels

Roberta J.C. da Fonseca, Guilherme Fraga, Fatmir Asllanaj, Francis H.R. França

A new development for the WBW model at elevated pressure levels

Roberta J. C. da Fonseca[a,*], Guilherme C. Fraga[a], Fatmir Asllanaj[b], F. H. R. França[a]

[a] *Universidade Federal do Rio Grande do Sul, Mechanical Engineering Department, Porto Alegre, Brazil*
[b] *Université de Lorraine, CNRS, LEMTA, F-54000 Nancy, France*

Abstract

This paper proposes an approach to obtain correlations for high pressure conditions for the weighted-sum-of-gray-gases (WSGG) model. The proposed formulation, which extends the wide-band based WSGG (WBW) model, entails solving the gray gas coefficients by partitioning the spectrum into a series of spectral intervals, and then using the classic version of the WSGG model to individually solve each segment. The line-by-line (LBL) method is used in the WBW model to first calculate the emittance of each band in which the spectra was divided. Polynomial temperature fits are then employed to compute the temperature and pressure-absorption coefficients. The sum of the contributions from every spectral band individually yields the overall radiative heat source and radiative heat flux. Showing deviations in most cases less than 5 % concerning the benchmark solution, the results demonstrate that, even at high pressures, the proposed method is capable to accurately resolve the radiative transfer.

Keywords: radiative transfer, participating medium, spectral models, wide-band models, high pressures

*Corresponding author
Email address: roberta.fonseca@ufrgs.br (Roberta J. C. da Fonseca)

1. Introduction

In combustion processes, which occur at elevated temperatures, the thermal radiation is frequently the principal mechanism of heat transfer because of the soot and participating gases formation [1]. The modeling of radiation in combustion processes under atmospheric conditions is already a very arduous task, however in scenarios at high pressure, it can become considerably more difficult [2]. Nevertheless, despite of the challenges, studies involving combustion at high pressures have recently gained attention [3–6], since strict environmental regulations, motivated by worries about global warming, urge the adoption of protocols in an effort to lessen the release of emission pollutant resulting from the burning of fossil fuels [7].

Rockets, gas turbines and piston engines are only a few examples of combustion systems that work at high pressures higher [2]. Oxy-combustion is another example of high pressure combustion, which is employed to capture and storage carbon [8]. Accurately describing the participating medium's radiative transfer is essential for optimizing combustion processes, particularly those that take place at elevated pressures, which present a higher computational cost in comparison to those that occur at atmospheric pressure. The total pressure system is also influenced by thermal radiation. As the radiation absorption rises with the total pressure and that the pressure also influences the chemical reactions, this significance increases at high pressures [9]. The increase in the soot production is the main way that soot radiation impacts the chemical reactions and is highly dependent on the pressure [2].

Transitions in vibrational and rotational energy states produce spectral lines centered around specific wavenumbers that are responsible for the absorption and emission of gases' thermal radiation. The generation of the properties of the gases with a high level of detail is achievable with high-resolution databases, as the HITEMP [10] and HITRAN [11], for instance. The entire radiation spectrum of gaseous species can include millions of spectral lines, each of which has its own dependence regarding the thermodynamic conditions (total pressure, temperature

and molar composition of the gases involved). The LBL benchmark solution [12] of the RTE, which takes into account each of these lines, allows for the calculation of thermal radiation with great accuracy. However, this methodology entails prohibitive computational costs for most real applications in engineering. Therefore, the advancements of accurate spectral models for the RTE solution is of great interest [13].

A great number of global spectral models, including the full-spectrum correlated-k (FSCK) method [14] and the spectral line-based WSGG (SLW) model [15], were developed with the intention of fastly and accurately determining the properties of the chemical species. Among them, the WSGG model [16] is the simplest, and perhaps the most widely used even as of today. In the WSGG model, the radiative intensity integration over all the wavenumbers is substituted by a sum over the partial intensities associated to each gray gas, and the erratic behavior of the spectrum of the participating medium is substituted by a little group of gray gases that occupy not necessary uninterrupted, fixed portions of the spectrum, for which the RTE is solved separately. In addition to being suitable for numerical calculations in engineering, the simplicity of the WSGG model allows it to save computational resources and ensure computational accuracy [17]. It can also be combined with computational fluid dynamics (CFD) solvers in order to resolve practical problems, having been recently applied by Refs. [18–20].

While atmospheric pressure conditions have generally yielded satisfactory results for the WSGG model [21–31], there are only a few applications of the model to high pressure combustion [3, 5, 32]. Since there are few WSGG correlations available at high pressures, some authors have attempted unsuccessfully to use these coefficients to high pressures scenarios, but they had obtained unsatisfactory results [33–35]. In high pressure situations, the WSGG coefficients are commonly applied at pressures between 1 atm and 40 atm [3, 4, 36, 37]. Above 40 atm, the WSGG model was studied by [5, 6].

As an alternative to the radiative calculation at high pressures, Paul et. al [38] proposed a simplified stepwise-gray spectral model, under the premise that

the smoothing of the absorption spectrum as the total pressure increases would allow the use of a band model, which is easier to implement into code than global models. A similar band mode was developed and tested by Johnson et al. [39]. When compared to the benchmark solution, the obtained results from other spectral models, including the SLW, SNB, SNBCK and FSK, were likewise extended to high pressure scenarios and showed satisfactory accuracy. The SLW model, for instance, was applied to pressures in the range of 0.1 atm and 50 atm by Refs. [40, 41] for participating media composed of H_2O, CO_2 and CO, and for jet diffusion flames ranging from atmospheric pressure up to 30 atm by [35]. The FSK method was studied at high pressures by [33–35, 42–45] providing accurate solutions. For systems subjected to total pressures over 30 atm, the SNBCK model presented maximum deviations of 2.5 % in relation to the SNB model [33–35, 43].

The current work's purpose is to bring a formulation for the WSGG model's high-pressure coefficient generation. The current approach is predicated on the WBW model [31]—originally developed for 1 atm—, where each spectral interval's contribution is solved using the standard WBW model after the spectrum is segmented into a series of intervals. It is worth highlighting that the WBW approach is distinguished from the standard WSGG model in the sense that rather than dealing with the entire radiation spectrum at once, every spectral interval that the spectrum was split up into is individually solved and then, to get the overall result, summed the contributions of each segment. The objective here is to present a methodology which is fast and accurate with a respectable offering between computational cost and accuracy. Expressed by the radiative heat flux and radiative heat source, the accuracy results found through the present method are tested against the solutions obtained via WSGG parameters of Ref. [3] and LBL benchmark integration.

2. Radiation modeling

2.1. LBL integration method

The solution of thermal radiation in participating media is based on solving the RTE along a given trajectory, which it can be expressed as [1, 13]:

$$\frac{\mathrm{d}I_\eta}{\mathrm{d}s} = -\kappa_\eta I_\eta + \kappa_\eta I_{b\eta}\,, \tag{1}$$

in which κ_η indicates the spectral absorption coefficient of the gas (or of a gaseous mixture), I_η represents the spectral radiation intensity and $I_{b\eta}$ is the spectral blackbody radiation intensity at the temperature of the medium at the position s. On the right-hand side of the RTE, the first term corresponds to the reduction in the radiation intensity due to absorption, and the second one expresses the mechanism of emission. In Eq. (1), the scattering of radiation is neglected, which is fully justified in media formed by participating species.

In the present study, non-uniform temperature and concentration distributions describe the participating medium formed by a H_2O-CO_2 mixture. The absorption coefficient is obtained according to the relation below

$$\kappa_\eta = NYC_\eta\,. \tag{2}$$

In the above equation, C_η is the absorption cross-section, Y is the mole fraction of the participating species and N is the molar density of the gas. The construction of the absorption spectra of the combustion byproducts, considering the collision broadening, is based on the Lorentz profile [1, 13]

$$C_\eta = \sum_{m=1}^{M} \frac{S_m}{\pi} \frac{\gamma_m}{\gamma_m^2 + (\eta - \eta_m)^2}\,, \tag{3}$$

in which S_m is the m-th line integrated intensity, γ_m is the line half-width, η_m is the line location and M is the amount of lines that make up the spectrum. The parameter γ_m is calculated accounting for the pressure and temperature according to [10]

$$\gamma_m = \left(\frac{T_{\mathrm{ref}}}{T}\right)^n p_e \gamma_{\mathrm{self,m}} + (p - p_e)\gamma_{\mathrm{air,m}}\,, \tag{4}$$

where p_e is the partial pressure of the participating species e, γ_{self} and γ_{air} are the half-widths considering the collision of gas molecules with each other and with air molecules, respectively, and n is the temperature-dependent coefficient. The values of S, γ_{air}, γ_{self} and n are obtained from a molecular spectroscopic database.

In solving the energy equation, the thermal radiation can be incorporated as a volumetric source term, directly related to the radiative flux divergence. Solving for the spectral radiation intensity using Eq. (1), the radiative heat flux (q_r) divergence at each position of the medium can be determined using the expression below:

$$\boldsymbol{\nabla} \cdot \vec{q_r} = \int_{\eta=0}^{\infty} \int_{\omega_l=0}^{4\pi} [-\kappa_\eta I_\eta + \kappa_\eta I_{b\eta}] \, \mathrm{d}\omega_l \, \mathrm{d}\eta \ . \tag{5}$$

For the radiative heat flux divergence to be determined, it needs two forms of integration. The first one corresponds to the spatial integration, which involves both the integration of Eq. (1) in a given direction, and the integration of Eq. (5) in all directions in the solid angle $\mathrm{d}\omega_l$. There are several spatial numerical methods, including P-N approximations, discrete ordinates method, zonal method, Monte Carlo etc. Despite the complexity of the problem, the spatial integration methods are well-established and can be found in specialized texts on thermal radiation [1, 13]. The second integration corresponds to the spectral integration of Eq. (3), which corresponds to the sum of the radiative energy at each wavenumber η. The gas absorption coefficients present a very complex behavior in relation to the wavenumber, and may be made up of millions of absorption lines. However, the greatest difficulty lies in how the thermodynamic state influences κ_η, which is even more critical in combustion processes.

2.2. WSGG model

The WSGG model considers that the absorption spectrum of a gas can be divided into a gray gases set and transparent windows. In this spectral model, the distribution of κ_η is normalized by the partial pressure p_a of the participating gases, $\kappa_{p\eta} = \kappa_\eta / p_a$, for the gray gases 1 to J, distributed non-contiguously

along the wavenumber, with no overlap between them. Under this assumption, the total emittance of the medium for a path-length L can be written as

$$\varepsilon = \sum_{j=1}^{J} a_j(T) \left[1 - \exp(-\kappa_{p,j} p_a L)\right] , \tag{6}$$

where the total of the chemical species' partial pressures that form the gaseous mixture is denoted by p_a, $a_j(T)$ represents the portion of blackbody energy emanating from the spectrum's sections in which $\kappa_{p\eta} = \kappa_{p,j}$; in the above equation, $\kappa_{p\eta} = \kappa_\eta / p_a$ represents the pressure-dependent spectral absorption coefficient. In practice, the above equation corresponds to an interpolation function of total emittance data of the medium, where generally, but not necessarily, the coefficients $\kappa_{p,j}$ are considered constant and a_j is represented by polynomial functions of the temperature. The determination of the total ε depends on the integration of the spectral emittance, such that

$$\varepsilon = \frac{\int_0^\infty \varepsilon_\eta I_{b\eta} \left[1 - \exp(-\kappa_{p\eta} p_a L)\right] \mathrm{d}\eta}{\int_0^\infty I_{b\eta} \, \mathrm{d}\eta} . \tag{7}$$

The integration of the RTE leads to

$$\frac{\mathrm{d}I_j}{\mathrm{d}s} = -\kappa_{p,j} p_a I_j + \kappa_{p,j} p_a a_j I_b , \tag{8}$$

in which I_b represents the total blackbody radiation intensity. The overall intensity can be determined by summing the individual intensities obtained for each one of the gray gases,

$$I = \sum_{j=0}^{J} I_j . \tag{9}$$

Despite its simplifications regarding the real spectrum of the gases, the WSGG model proved capable of generating results with very satisfactory accuracy in a set of problems with elevated temperature and concentration gradients of the involved species, similar to those found in combustion processes [4, 6, 18, 19, 46].

2.3. WBW model

In spite of its simplicity by representing the spectrum commonly with only four gray gases ($J = 4$), the WSGG model is capable of obtaining solutions with

very satisfactory accuracy in relation to the application of the LBL integration method, typically with maximum local errors below 10 % and average deviations below 5 %. The computational time of the WSGG model is much lower than that needed by the LBL benchmark solution, in the order of 0.001 %. The SLW and FSK global models typically have greater accuracy than the WSGG model, but they are more complex and require around five times more computational time. Considering the long time needed to solve the RTE in problems in which the thermal radiation is just one of the phenomena involved, such as in combustion problems, the WSGG model may be a good option when the uncertainties introduced by other phenomena are greater than those of the model itself. Because of this, the present study proposes a new methodology for the WSGG model, which consists of applying the WBW model [31] for total pressures above the atmospheric (i.e., above 1 atm). By segmenting the spectrum into a series of M bands of width $\Delta\eta_m$, the proposed method seeks to widen the the standard WSGG model accuracy using its assumptions by calculating the contributions of all bands individually. The number J_m of gases in each band does not necessarily need to be the same, this being an aspect that allows optimization, i.e., using a greater or lesser number of gray gases in a interval according to their importance in the global calculation. The results of each band are added together to calculate the total quantities.

The emittance of the m-th band can be calculated by use the LBL method of the spectral data extracted from HITEMP 2010 according to the following equation

$$\varepsilon_m = \frac{\int_{\Delta\eta_m} I_{b\eta}\left[1-\exp(-\kappa_{p\eta}p_a L)\right]\mathrm{d}\eta}{\int_{\Delta\eta_m} I_{b\eta}\,\mathrm{d}\eta}\,, \tag{10}$$

where $\int_{\Delta\eta_m} I_{b\eta}\,\mathrm{d}\eta = f_m I_b$, in which f_m is the blackbody energy fraction that emanates from each spectral band $\Delta\eta_m$ and is calculated using the distribution of Planck [1, 13]. With the aforementioned definition, the emittance of a band ε_m can reach a maximum value of 1, as well as the total emittance defined in Eq. (7), which are related as $\varepsilon = \sum_{m=1}^{M} f_m\varepsilon_m$.

With the other WBW assumptions being equivalent to those of the WSGG

model, for each band the value of ε as follow as

$$\varepsilon_m = \sum_{j=1}^{J_m} a_{j,m}(T)\left[1 - \exp(-\kappa_{p,j,m} p_a L)\right] , \tag{11}$$

in which $a_{j,m}$ is the temperature-dependent coefficient, $\kappa_{p,j,m}$ is the pressure-dependent coefficient—both related to the gray gas j and band m. Finally, as in the classic model, the coefficients of the WBW model are determined by correlating Eq. (11) with the values of emittance of the bands calculated via LBL integration of Eq. (10), considering the coefficients $\kappa_{p,j,m}$ as constant and the coefficients $a_{j,m}$ are represented by temperature polynomial functions.

The RTE, in the context of the proposed method, is given by

$$\frac{\mathrm{d}I_{j,m}}{\mathrm{d}s} = -\kappa_{p,j,m} p_a I_{j,m} + \kappa_{p,j,m} p_a a_{j,m} f_m I_b \, , \tag{12}$$

where the blackbody energy emission in the wide-band m is weighted by f_m, the overall radiation intensity is computed as the total of the individual intensities calculated for each gray gas j, according to the equation below

$$I = \sum_{m=1}^{M} \sum_{j=0}^{J} I_{j,m} \, , \tag{13}$$

and $a_{j,m}$ is fitted using a temperature polynomial function

$$a_{j,m}(T) \; = \; \sum_{k=0}^{\mathcal{K}} b_{j,m,k} T^k \, , \tag{14}$$

with $b_{j,m,k}$ displaying the coefficients of the temperature polynomial of the order k for the gray gas j and band m. In a participating medium enclosed by boundaries that are black, Eq. (12) is constrained by the boundary condition: $I_{j,m}\big|_{\text{wall}} = (a_{j,m} f_m I_b)\big|_{\text{wall}} = a_{j,m}(T_w) f_m(T_w) I_b(T_w)$. The terms of the boundary condition are all evaluated in relation to the wall temperature T_w, which, in the present paper, is prescribed for all test cases investigated here.

Finally, by integrating the RTE and resolving the intensities for n_d directions,

q_r and radiative heat source, S_r, at each point can be computed as

$$q_r(x) = \sum_{m=1}^{M} \sum_{l=1}^{n_d} \sum_{j=0}^{J} 2\pi\mu_l\omega_l \left[I^+_{j,l,m}(x) - I^-_{j,l,m}(x) \right] , \tag{15}$$

$$S_r(x) = \sum_{m=1}^{M} \sum_{l=1}^{n_d} \sum_{j=1}^{J} 2\pi\kappa_{pj,m} p_a \omega_l \left[I^+_{j,l,m}(x) + I^-_{j,l,m}(x) \right] - 4\pi\kappa_{pj,m} p_a a_{j,m} f_m I_b(x) , \tag{16}$$

in which $I^-_{j,l,k}$ and $I^+_{j,l,k}$ are the gray gas radiation intensities in the negative and positive directions, respectively, ω_l are the weights of the quadrature and μ_l are the direction cosines. The full WBW model formulation is available in [31] for a more thorough understanding.

3. Results and discussions

In the present paper, the formulation is implemented to a 1D system, in which the plates are black and separated by $X = 1\,\text{m}$, illustrated in Fig. 1. The fixed mole fraction of the medium is $p_w/p_c = 2$ and it experiences three total pressures: 1 atm, 10 atm and 20 atm. Using the direction cosines and weights presented in Ref. [47], the RTE directional integration was completed via discrete ordinates method for 8 directions; 200 equally spaced cells were used for the discretization of the computational domain spatial mesh. These parameters were chosen through complementary studies analyzing the quality of the spatial and directional meshes, which demonstrated that a higher level of refinement had no impact on the accuracy of the solutions, so that the values adopted for the problem under study were considered adequate. As shown in Table 1, five spectral bands was the quantity of divisions into which the spectrum was fractioned. The criteria to establish the division of the bounds of each band are the same used by Refs. [31, 48]. Fixed mole fractions of $Y_c = 0.1$ and $Y_w = 0.2$ (with the letters c and w standing for carbon dioxide and water vapor, respectively), and 43 values of L (ranging from 0.001 m up to 30 m) were adopted to generate the band emittances. Although the WBW model, in its your original formulation, has already provided correlations for the case in which the total pressure is 1 atm

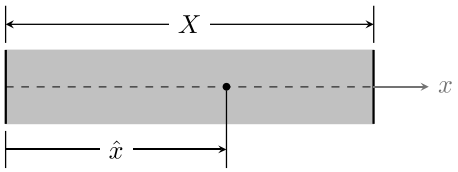

Figure 1: Schematic of the computational domain.

Table 1: Bounds of the spectral bands evaluated in this paper.

Spectral band	η_l [cm^{-1}]	η_u [cm^{-1}]
1	0	1000
2	1000	2600
3	2600	4400
4	4400	6000
5	6000	10000

through Ref. [31], new coefficients were produced for this value of p, since the upper limit of the final interval in that paper was different from the case under study here. Due to the similarity between the coefficients proposed by [31], even though the last spectral band is slightly different, it was decided to omit the WBW coefficients for 1 atm. For the other values of total pressure under study here, the WBW correlations are available in Appendix A.

The temperature and medium composition profiles are described by a set of cases. Case 1 presents simple symmetry regarding the x-axis, and its behaviors for the temperature profile and mole fraction of carbon dioxide are expressed, respectively, as

$$T(\hat{x}) = 400 + 1400 \sin^2(\pi \hat{x}) , \tag{17}$$

$$Y_c(\hat{x}) = 0.1 \sin^2(\pi \hat{x}) , \tag{18}$$

where the parameter $\hat{x}$ represents the dimensionless distance relative to the left boundary ($\hat{x} = x/X$). In the second case, T and Y_c present double symmetry,

and these two quantities are described, respectively, by

$$T(\hat{x}) = 400 + 1400\sin^2(2\pi\hat{x}), \tag{19}$$

$$Y_c(\hat{x}) = 0.1\sin^2(2\pi\hat{x}). \tag{20}$$

The profiles described in Eqs. (17) and (19) have a maximum value of temperature at 1800 K and an average temperature of 1100 K. In Eqs. (18) and (20) the peak of carbon dioxide mole fraction is 0.1 and the value average of the medium composition is 0.05. Another set of temperature is also tested, but with the average and maximum temperatures of 1300 K and 2200 K, respectively, as follows

$$T(\hat{x}) = 400 + 1800\sin^2(2\pi\hat{x}), \tag{21}$$

$$T(\hat{x}) = \begin{cases} 880 + 1320\sin^2(2\pi\hat{x}), \text{if } \hat{x} \leq 0.25, \\ 400 + 1800\left\{1 - \sin^{\frac{3}{2}}[\frac{2\pi}{3}(\hat{x} - 0.25)]\right\}, \text{if } \hat{x} > 0.25. \end{cases} \tag{22}$$

Regarding the above profiles, Case 3 combines Eqs. (18) and (21) for CO_2 mole fraction and temperature profiles, respectively. Finally, Case 4 is represented by Eqs. (20) and (22) for the carbon dioxide mole fraction and temperature profiles, respectively. In Cases 1 to 3, both walls are at a temperature of 400 K. In Case 4, the left boundary is at 880 K while the right wall is at 400 K.

With the objective of optimizing the computational cost required to generate the results for the WBW model, the quantity of gray gases spread within each segment in the four test cases under investigation in this paper was varied between the values of two and four. It was decided to adopt this quantity of gray gases in each spectral interval based on the study carried out by [31], in which it was found that it is appropriate to distribute a greater number of gases to the most important bands and a smaller number to the less important ones. In Approach A, a total of 20 gray gases are distributed across the five bands. In Approach B, 14 gases are used to represent the proposed method. And, in Approaches C and D, are distributed a total of 12 and 16 gray gases, respectively, along the spectrum. Further, the results obtained by Approaches

Table 2: Gray gases quantity in each interval for each one of the tested WBW approaches.

Approach	Band 1	Band 2	Band 3	Band 4	Band 5	Total
A	4	4	4	4	4	20
B	2	4	4	2	2	14
C	2	3	3	2	2	12
D	2	3	3	4	4	16

A–D are obtained through combinations of the sets of correlations presented in Appendix A. Table 2 presents a summary with the number of gray associated to each band for each approach.

To measure the accuracy of the proposed formulation regarding the LBL method, maximum and average normalized deviations were calculated, according to the equation below:

$$\delta\phi = \frac{|\phi_{\mathrm{LBL}} - \phi_{\mathrm{app}}|}{\max(|\phi_{\mathrm{LBL}}|)} \times 100\% \,. \tag{23}$$

In the above equation, ϕ is either q_r and S_r, the subscript "app" indicates the tested approach against the LBL method (indicated by the subscript "LBL"), and $\max(|\phi_{\mathrm{LBL}}|)$ represents the maximum absolute value for q_r or S_r obtained by the reference solution. Later, the maximum and average deviations in relation to the benchmark solution will be indicated by the use of the subscripts "max" and "avg", respectively.

Using the methodology outlined in Ref. [3], the absorption spectra of CO_2 and H_2O at high pressures were generated from the HITEMP 2010. All five of the intervals' emittances were obtained via Eq. (10), and the adjustments of ε were completed in an analogous way to that reported in Ref. [31]. The function presented in Eq. (11) was employed in order to fit the proposed model's parameters. As in Ref. [31], the WBW correlations were generated assuming a number between two and four to describe the amount of gray gases in each band, adopting a polynomial of fifth order to describe the dependence on temperature. The emittance charts for 10 atm and 20 atm are shown in Figs. 2 and 3. The ε

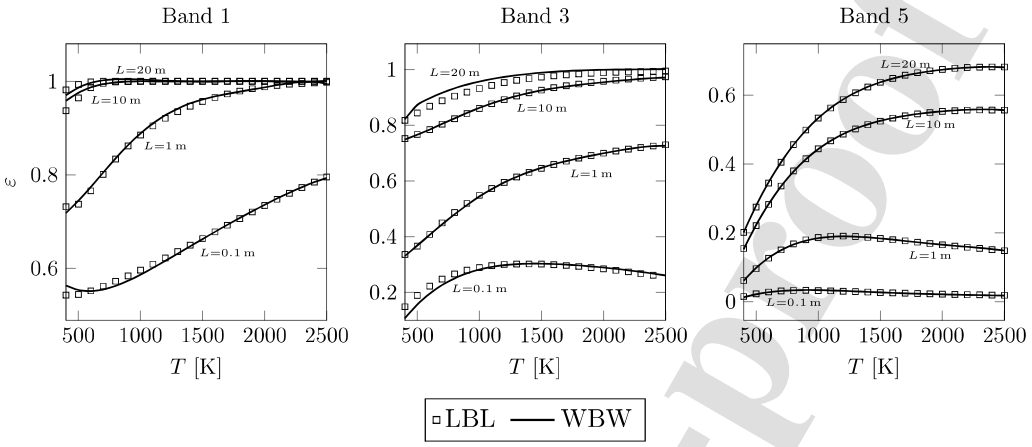

Figure 2: Emittances of three of the selected bands and $p = 10\,\text{atm}$.

values depicted in these figures illustrate the solutions found with the WBW model considering four gray gases per interval. Only 4 of the values of L that were used to calculate ε were displayed in the figures for the sake of brevity; the remaining path-lengths exhibit tendencies that are similar to what is addressed next.

At a total pressure of $p = 10\,\text{atm}$, the results illustrated in Fig. 2 demonstrate a good fit between the WBW model and the LBL integration method, with a maximum relative error (determined as $|\varepsilon_{\text{LBL}} - \varepsilon_{\text{WBW}}|/\varepsilon_{\text{LBL}} \times 100\%$) of less than 2 %, occurring in the areas with cooler temperatures. Given that the WBW model outperformed the benchmark solution, the polynomial fitting is deemed adequate for the purposes of this paper's analysis.

The emittances for the three bands produced using the WBW model and the LBL method for $p = 20\,\text{atm}$ are compared in Fig. 3. At contrast to $p = 10\,\text{atm}$, 2.1 % was the maximum local deviation found at the temperature-highest region, where the biggest disparity between the two methods was observed. Despite the omission of ε results for 1 atm, the deviations for the other values of total pressure are comparable to those that were disclosed by [31], corroborating the suitability of the polynomial fitting.

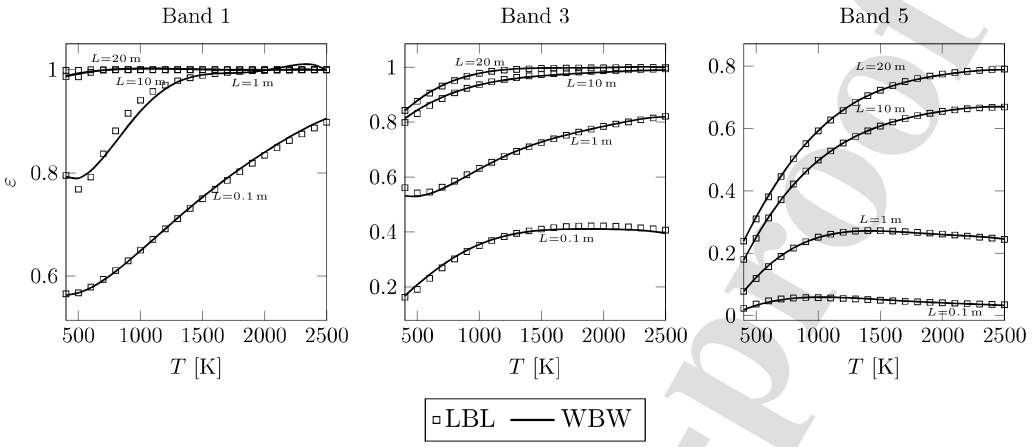

Figure 3: Emittances of three of the selected bands and $p = 20\,\text{atm}$.

The WBW model is now used to calculate q_r and S_r for the four case studies that were described. The pressures of 1 atm to 20 atm are displayed in the following figures together with q_r and S_r for each case. Calculations for atmospheric pressure were carried out with the WBW model coefficients presented in [31], but with new correlations generated for the last spectral band. The results obtained by applying the WBW model, assuming that there are two to four gray gases in each spectral band, are plotted in Figs. 4–7. Additionally, under the identical physical conditions, these diagrams show the resulting curves produces by applying the WSGG coefficients that were generated by [3]. The goal is to assess whether the proposed methodology's accuracy might be improved upon in comparison to an alternative WSGG model formulation for high pressures that is currently existing in the literature. Tables 3 and 4 provide a summary of the average and maximum normalized errors with the LBL method in comparison to the WSGG and WBW models, respectively. In order not to impair the understanding of the figures with the results, only the curves that describe the solutions containing four gray gases in each band were plotted in Figs. 4–7 (curves "WBW-A" in these figures). The performance of the other solutions (Approaches B to D) are expressed only in terms of maximum

and average errors regarding the reference solution and can be seen in Table 4.

Figure 4 presents q_r and S_r results for Case 1 for the WBW and WSGG approaches against the LBL integration for the three total pressures assessed in this paper. When comparing the two methods studied in this paper with respect to the LBL solution, a good agreement is found between the WBW model and the LBL method throughout the three total pressure values for q_r and S_r. Although the atmospheric pressure does not characterize a high pressure scenario, it was decided to also present the results obtained with 1 atm, so that the performance of the proposed method could be evaluated as the value of the total pressure system rises. Thus, for 1 atm, Table 3 shows that the biggest errors obtained via WSGG model of Ref. [3] for 1 atm are 5.1 % and 3.2 %, respectively. According to Table 4, all the four approaches of the WBW model presented a better performance for the atmospheric pressure in comparison with the WSGG model. The results with greater accuracy were obtained with the Approach A of the WBW model, with maximum errors of 3.0 % for q_r and 3.4 % for S_r. With Approach C, which presents 12 gray gases distributed throughout the spectrum, the WBW model also presented smaller deviations compared to the WSGG model, with maximum errors of 4.1 % (q_r) and 3.1 % (S_r). For $p = 10$ atm, the WSGG model provides maximum errors of 5.6 % and 3.8 % for q_r and S_r, respectively. With the WBW model, the Approaches B and D carried out to the best results, such that: for q_r, the maximum errors were 1.8 % (Approach B) and 1.3 % (Approach D); for S_r, the maximum deviations were 0.7 % (Approach B) and 0.6 % (Approach D). For 20 atm, the maximum deviations with the WSGG model were 3.4 %, for q_r, and 3.8 %, for S_r. Again, all the tested WBW approaches presented a superior accuracy compared to the WSGG model, with the Approaches A and C reaching the most accurate results: 1.4 % and 1.35 % for the radiative heat flux, respectively, and 0.6 % and 0.7 % for the radiative heat source, respectively. These results show that highlight the fact that optimizing the gray gases number distributed in each interval can further improve the results, which were already better than those obtained through the WSGG correlations proposed by Ref. [3].

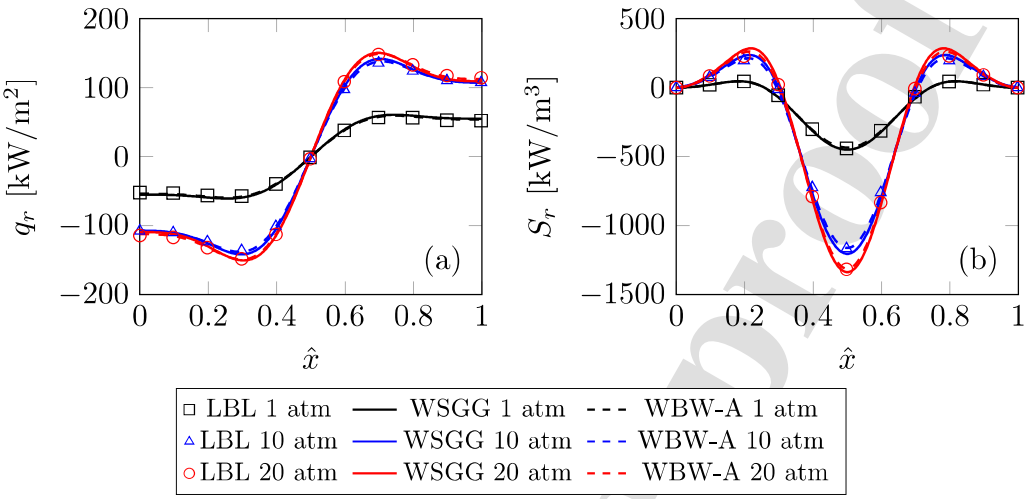

Figure 4: Case 1: (a) radiative heat flux; (b) radiative heat source.

Table 3: Percentage deviations of q_r and S_r between the WSGG model of Ref. [3] and the reference solution.

	$p = 1$ atm [%]				$p = 10$ atm [%]				$p = 20$ atm [%]			
	$(\delta q_r)_{\max}$	$(\delta q_r)_{\text{avg}}$	$(\delta S_r)_{\max}$	$(\delta S_r)_{\text{avg}}$	$(\delta q_r)_{\max}$	$(\delta q_r)_{\text{avg}}$	$(\delta S_r)_{\max}$	$(\delta S_r)_{\text{avg}}$	$(\delta q_r)_{\max}$	$(\delta q_r)_{\text{avg}}$	$(\delta S_r)_{\max}$	$(\delta S_r)_{\text{avg}}$
Case 1	5.10	3.67	3.22	1.38	5.61	2.39	3.80	2.14	3.37	1.83	3.82	1.61
Case 2	5.24	2.50	6.21	1.97	5.51	3.32	8.08	2.71	7.09	3.10	7.95	2.96
Case 3	7.20	3.47	7.54	2.47	5.27	2.13	3.74	1.61	5.48	3.22	6.44	2.33
Case 4	10.36	5.41	7.42	1.74	4.13	1.75	4.73	1.01	5.22	2.28	5.48	1.22

For Case 2, Fig. 5 displays q_r and S_r for each one of the three total pressure values. Once again, there was a good match between the LBL and WBW solutions, with the latter performing superior to the WSGG model, since, the Case 1, the proposed method showed the least inaccuracy with respect to the LBL integration. Based on Tables 3 and 4, for 1 atm, the maximum deviations were obtained with the Approaches A and B, being 3.6 % and 4.1 %, respectively, for q_r, and 4.0 % and 3.7 %, respectively, for S_r, against 5.2 % (q_r) and 6.2 % (S_r) via WSGG approach. For 10 atm, the Approaches C and D presented the best performances, with maximum deviations of 2.6 % and 2.0 %, respectively,

Table 4: Percentage deviations of q_r and S_r between the proposed method and the reference solution.

	$(\delta q_r)_{\max}$	$(\delta q_r)_{\text{avg}}$	$(\delta S_r)_{\max}$	$(\delta S_r)_{\text{avg}}$	$(\delta q_r)_{\max}$	$(\delta q_r)_{\text{avg}}$	$(\delta S_r)_{\max}$	$(\delta S_r)_{\text{avg}}$
	WBW Approach A [%]				WBW Approach B [%]			
$p = 1$ atm								
Case 1	3.03	1.87	3.36	1.09	3.59	2.30	3.17	1.01
Case 2	3.60	1.50	4.04	1.54	4.09	1.76	3.73	1.38
Case 3	4.06	1.77	6.02	2.46	4.70	2.10	5.05	2.19
Case 4	4.16	2.57	6.25	1.45	4.72	2.21	5.99	1.36
$p = 10$ atm								
Case 1	2.01	0.89	1.78	0.68	2.11	1.24	1.26	0.59
Case 2	2.81	1.17	2.47	0.95	2.89	1.22	2.41	0.90
Case 3	5.28	2.13	3.67	1.55	6.90	2.99	2.88	1.38
Case 4	4.35	2.34	4.67	1.34	6.61	3.61	4.38	0.64
$p = 20$ atm								
Case 1	1.37	0.63	2.11	0.70	1.35	0.73	2.14	0.66
Case 2	2.41	0.78	4.66	1.39	1.85	1.04	4.43	1.24
Case 3	2.88	1.18	4.16	1.47	2.48	0.84	3.67	1.23
Case 4	3.23	1.24	4.44	0.81	4.86	1.08	5.04	1.34
	WBW Approach C [%]				WBW Approach D [%]			
$p = 1$ atm								
Case 1	4.13	2.95	3.09	1.17	3.96	2.78	3.05	1.13
Case 2	5.42	2.42	4.31	1.84	5.26	2.33	4.06	1.80
Case 3	4.93	1.87	4.01	1.42	4.53	1.65	3.95	1.33
Case 4	6.65	4.68	4.70	1.11	8.73	4.29	4.60	1.11
$p = 10$ atm								
Case 1	1.53	0.90	1.62	0.49	1.60	0.67	2.23	0.82
Case 2	2.62	0.99	1.99	0.85	2.04	0.73	2.22	1.03
Case 3	5.15	2.19	3.76	1.11	3.07	1.17	2.27	0.86
Case 4	4.20	2.24	4.38	0.80	1.92	0.86	3.35	0.70
$p = 20$ atm								
Case 1	0.82	0.39	1.23	0.48	2.35	1.56	3.06	0.99
Case 2	1.92	0.90	2.86	0.84	2.50	0.58	3.42	1.03
Case 3	3.50	1.62	2.05	0.94	1.84	0.75	3.31	1.32
Case 4	2.93	1.10	2.36	0.60	2.85	0.76	3.45	0.90

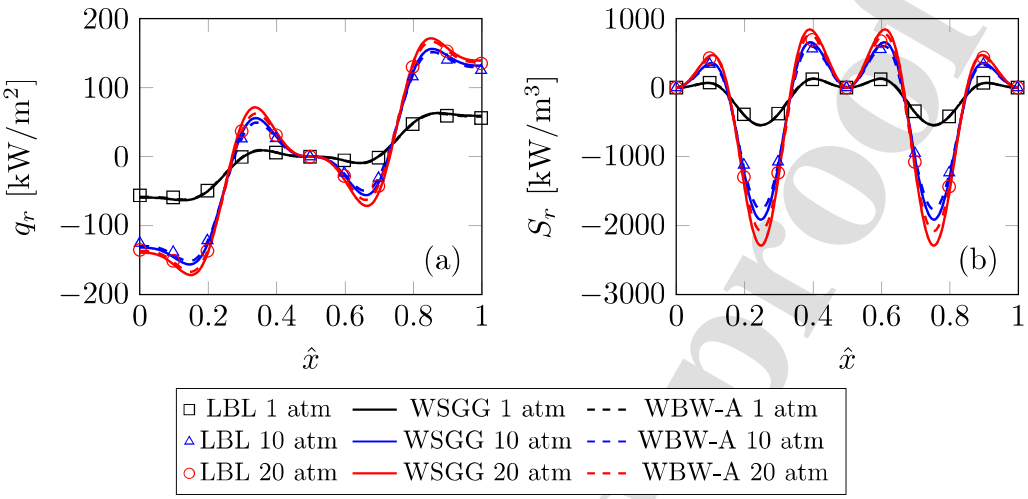

Figure 5: Case 2: (a) radiative heat flux; (b) radiative heat source.

for q_r, and 2.0 % and 2.2 %, respectively, for S_r. The WSGG model, in turn, reached maximum deviations of 5.5 %, for q_r, and 8.1 %, for S_r. For the third value of total pressure tested in this paper (i.e., 20 atm), the Approaches B and C carried out to the smallest errors, whose magnitudes of deviations for q_r and S_r were 1.8 % and 4.4 %, respectively, with the first one, and 1.9 % and 2.9 %, respectively, with the second one. Meanwhile, the WSGG model, in turn, provided maximum errors of 7.1 % and 7.9 % for the radiative heat flux and radiative heat source, respectively. Again, the WBW solution demonstrated to be a superior substitute for calculating the radiative transfer compared to the standard WSGG model, since the results obtained with the proposed method presented more accuracy.

The results depicted in Fig. 6 show q_r and S_r for Case 3 for the three values of pressure under consideration. According to data from Table 3, for the three values of total pressure, the worst results were obtained for 1 atm, with maximum errors of 7.2 %, for q_r, and 7.5 %, for S_r. These deviations decrease with the increase of the total pressure, becoming 5.3 % and 3.7 %, for p =10 atm, and 5.5 % and 6.4 %, for p =20 atm. Regarding the WBW model, all the tested approaches

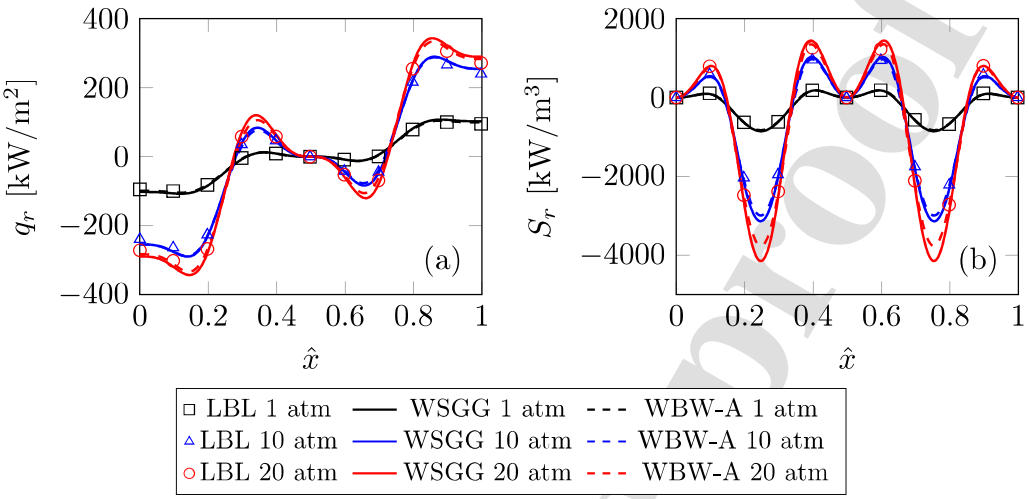

Figure 6: Case 3: (a) radiative heat flux; (b) radiative heat source.

performed better compared to the classic version of the WSGG model, since the discrepancies regarding the LBL solution were less than those calculated by the WSGG coefficients proposed by Ref. [3]. For 1 atm, the best performances of the WBW model were obtained with the Approaches C and D, with maximum deviations of 4.9 % and 4.5 %, respectively, for the radiative heat flux, and 4.0 % and 3.9 %, respectively, for the radiative heat source. For $p = 10$ atm, Approaches C and D presented the smallest deviations for the radiative heat flux, with magnitudes of 5.1 % and 3.1 %, respectively; for the radiative heat source, Approaches B and D reached the best results, with maximum deviations of 2.9 % and 2.8 %, respectively. For $p = 20$ atm, again Approaches C and D presented the best performances, being 3.5 % and 1.8 % the maximum errors obtained for q_r, and 2.0 % and 3.3 % the deviations for S_r, respectively.

Finally, Fig. 7 shows the results for q_r and S_r for Case 4 for all the analyzed values of total pressure. As in previous test cases, the proposed method outperformed the standard WSGG model. For the first value of total pressure evaluated (i.e., $p = 1$ atm), the maximum error for the radiative heat flux exceeded 10 %; for the radiative heat source, the performance of the WSGG model was not very

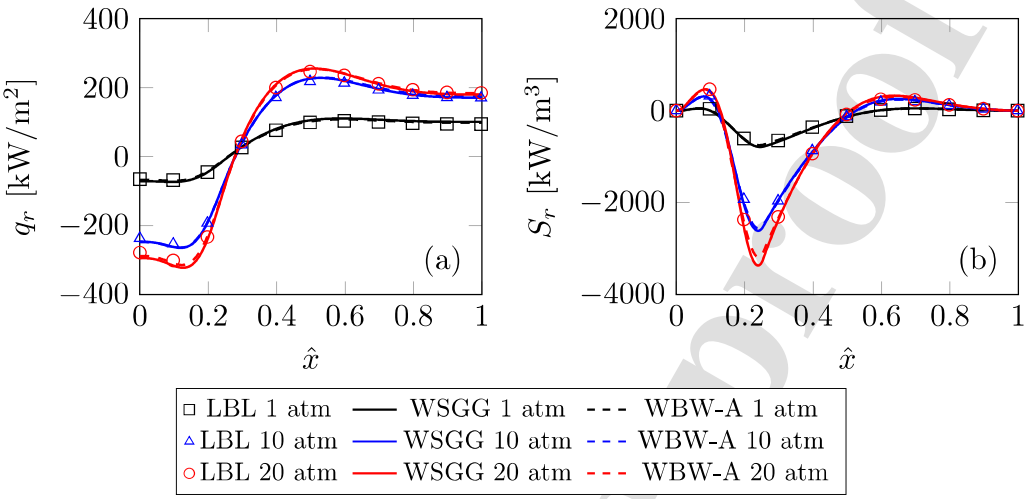

Figure 7: Case 4: (a) radiative heat flux; (b) radiative heat source.

good either, with 7.4 % of deviation. The results for the highest pressures, 10 atm and 20 atm, were slightly better, with maximum deviations whose magnitudes were 4.1 % and 5.2 %, respectively, for q_r, and 4.7 % and 5.5 %, respectively, for S_r. Analogously to what was observed with the WSGG model, Case 4 was the one that had the biggest errors regarding the LBL method, in contrast to the other test cases studied. Still, on average, the WBW model presented a better performance in comparison to the standard WSGG model. The Approaches A and B presented the smallest deviations, being 4.2 % and 4.7 %, respectively, for the radiative heat flux, and 6.6 % for both approaches, for the radiative heat source, for $p = 1$ atm. For the intermediate value of total pressure (i.e., $p = 10$ atm), the best performances were obtained by Approaches C and D, in which the maximum deviations 4.2 % (q_r) and 1.9 % (S_r), with the first one, and 4.4 % (q_r) and 3.3 % (S_r), for the second one. For the last value of total pressure (i.e., 20 atm), the smallest errors also were provided through Approaches C and D, whose the magnitudes were 2.9 % and 2.8 %, respectively, for q_r, and 2.4 % and 3.4 %, respectively, for S_r.

Additionally, it is important to highlight that the solution with 20 gray gases

(Approach A) is equivalent to a classic approach of the SLW model, which uses from 20 to 25 gases distributed throughout the entire spectrum. Therefore, by reducing from 20 to 12 gray gases, the WBW model will decrease the number of equations to be solved, which, in turn, reduces the computational time required to run the same test case. So, the Approach D, which in some cases led to the smallest deviations in relation to the benchmark solution, represents a significant reduction in the computational cost, since it will be necessary to solve the RTE only 12 times, i.e., once for each gray gas, instead of solving this equation 20 times. Thus, it is noted that the optimized approaches of the WBW model become competitive in relation to the SLW model, since the computational time required is less, in addition to having just as good accuracy. In future studies, it is planned to numerically compare optimized approaches of the WBW model with some formulations of the SLW model.

4. Conclusions

A WBW model extension for estimating the radiative transfer at high pressures was carried out in this paper. Based on the LBL data of the emittance for 1 atm to 20 atm, correlation sets for the proposed model were developed. The proposed method involves optimizing the standard WSGG model through the division of the spectrum into a series of segments. The results obtained with the model that was firstly proposed by [31] for atmospheric pressure showed that the WBW model can be successfully employed at high pressures scenarios, as evidenced by the deviations for the prediction of the emittance about 2 %. The accuracy of the present formulation was evaluated for four cases with non-uniform temperature and concentration CO_2/H_2O mixtures. The maximum errors were of the order of 5 % regarding the LBL integration for q_r and S_r. Although not very common, the worst results, whose errors exceeded 6 %, were in cases where even the standard WSGG model presented even lower performance. In addition, the tested approaches showed that one of the ways to improve the proposed formulation would be to carry out more in-depth studies to weight the

importance of the spectral bands, in order to optimize the gray gases quantity, leading to more accurate results with less computational time. Furthermore, new correlations are being produced for variable mole fraction ratios of water vapor and carbon dioxide, in order to increase the flexibility and applicability of the proposed model to larger variety of engineering problems. Apart from this, the fact of making the formulation adaptable and suitable to other combustion situations, new WBW coefficients are also being produced for different H_2O-CO_2 mole fraction ratios. Comparisons with other more advanced spectral models (such as SLW, FSCK etc.) could also be addressed in future studies. Another possibility for the continuity of the research is to apply the present WBW model in the solution of non-gray boundaries and high pressure conditions. This topic has already begun to be explored with the preliminary work of Ref. [49], in which the WBW model showed a higher accuracy than conventional box models, with maximum errors of 4 %, and which will be investigated in more detail in future studies.

Acknowledgements

Author RJCF thanks Conselho Nacional de Desenvolvimento Científico e Tecnológico (CNPq) for her fellowship postdoctoral. Author FHRF thanks CNPq for him research grant 302686/2017-7.

References

[1] M. F. Modest, Radiative Heat Transfer, Academic Press, 2013.

[2] M. F. Modest, D. C. Haworth, Radiative Heat Transfer in Turbulent Combustion Systems: Theory and Applications, Springer, 2016.

[3] F. R. Coelho, F. H. R. França, WSGG correlations based on HITEMP2010 for gas mixtures of H_2O and CO_2 in high total pressure conditions, International Journal of Heat and Mass Transfer 127 (2018) 105–114. doi:10.1016/j.ijheatmasstransfer.2018.07.075.

[4] B. Wang, Y. Xuan, An improved WSGG model for exhaust gases of aero engines within broader ranges of temperature and pressure variations, International Journal of Heat and Mass Transfer 136 (2019) 1299–1310. doi:10.1016/j.ijheatmasstransfer.2019.03.105.

[5] H. Bordbar, F. R. Coelho, G. C. Fraga, F. H. França, S. Hostikka, Pressure-dependent weighted-sum-of-gray-gases models for heterogeneous CO_2-H_2O mixtures at sub- and super-atmospheric pressure 173 (2021) 121207. doi:10.1016/j.ijheatmasstransfer.2021.121207.

[6] Q. Zhang, S. Shan, Z. Zhou, K. H. Luo, A new WSGG radiation model of CO/CO_2 mixed gas for solar-driven coal/biomass fuel gasification, Fuel 346 (2023) 128241. doi:10.1016/j.fuel.2023.128241.

[7] T. F. Wall, Combustion processes for carbon capture, Proceedings of the Combustion Institute 31 (1) (2007) 31–47. doi:10.1016/j.proci.2006.08.123.

[8] T. Wall, R. Stanger, S. Santos, Demonstrations of coal-fired oxy-fuel technology for carbon capture and storage and issues with commercial deployment 5 (2011) 5–15.

[9] Z. Chen, X. Qin, B. Xu, Y. Ju, F. Liu, Studies of radiation absorption on flame speed and flammability limit of CO_2 diluted methane flames at elevated pressures, Proceedings of the Combustion Institute 31 (2) (2007) 2693–2700.

[10] L. Rothman, I. Gordon, R. Barber, H. Dothe, R. Gamache, A. Goldman, V. Perevalov, S. Tashkun, J. Tennyson, HITEMP, the high-temperature molecular spectroscopic database, Journal of Quantitative Spectroscopy and Radiative Transfer 111 (15) (2010) 2139–2150. doi:10.1016/j.jqsrt.2010.05.001.

[11] I. Gordon, L. Rothman, R. Hargreaves, R. Hashemi, E. Karlovets, F. Skinner, E. Conway, C. Hill, R. Kochanov, Y. Tan, P. Wcisło, A. Finenko, K. Nelson,

P. Bernath, M. Birk, V. Boudon, A. Campargue, K. Chance, A. Coustenis, B. Drouin, J. Flaud, R. Gamache, J. Hodges, D. Jacquemart, E. Mlawer, A. Nikitin, V. Perevalov, M. Rotger, J. Tennyson, G. Toon, H. Tran, V. Tyuterev, E. Adkins, A. Baker, A. Barbe, E. Canè, A. Császár, A. Dudaryonok, O. Egorov, A. Fleisher, H. Fleurbaey, A. Foltynowicz, T. Furtenbacher, J. Harrison, J. Hartmann, V. Horneman, X. Huang, T. Karman, J. Karns, S. Kassi, I. Kleiner, V. Kofman, F. Kwabia–Tchana, N. Lavrentieva, T. Lee, D. Long, A. Lukashevskaya, O. Lyulin, V. Makhnev, W. Matt, S. Massie, M. Melosso, S. Mikhailenko, D. Mondelain, H. Müller, O. Naumenko, A. Perrin, O. Polyansky, E. Raddaoui, P. Raston, Z. Reed, M. Rey, C. Richard, R. Tóbiás, I. Sadiek, D. Schwenke, E. Starikova, K. Sung, F. Tamassia, S. Tashkun, J. Vander Auwera, I. Vasilenko, A. Vigasin, G. Villanueva, B. Vispoel, G. Wagner, A. Yachmenev, S. Yurchenko, The HITRAN2020 molecular spectroscopic database, Journal of Quantitative Spectroscopy and Radiative Transfer (2021) 107949doi:10.1016/j.jqsrt.2021.107949.

[12] J. Taine, A line-by-line calculation of low-resolution radiative properties of CO_2-CO-transparent nonisothermal gases mixtures up to 3000 K, Journal of Quantitative Spectroscopy and Radiative Transfer 30 (4) (1983) 371–379. doi:10.1016/0022-4073(83)90036-5.

[13] J. R. Howell, M. P. Mengüç, R. Siegel, Thermal Radiation Heat Transfer, 6th Edition, CRC press, 2016.

[14] M. F. Modest, H. Zhang, The full-spectrum correlated-k distribution for thermal radiation from molecular gas-particulate mixtures, Journal of Heat Transfer 124 (1) (2002) 30–38. doi:10.1115/1.1418697.

[15] M. K. Denison, B. W. Webb, A spectral line-based weighted-sum-of-gray-gases model for arbitrary RTE solvers, Journal of Heat Transfer 115 (4) (1993) 1004–1012. doi:10.1115/1.2911354.

[16] H. C. Hottel, F. Sarofim, Radiative Transfer, McGraw-Hill, 1967.

[17] P. Nakod, G. Krishnamoorthy, M. Sami, S. Orsino, A comparative evaluation of gray and non-gray radiation modeling strategies in oxy-coal combustion simulations, Applied Thermal Engineering 54 (2) (2013) 422–432. doi:10.1016/j.applthermaleng.2013.01.049.

[18] L. G. P. Rodrigues, I. M. Machado, A. Ziemniczak, F. M. Pereira, P. R. Pagot, F. H. R. França, Comparisons between numerical simulations and experimental measurements of radiative heat flux for a series of CH_4/N_2 diluted laminar non-premixed flames, Combustion Science and Technology 193 (1) (2021) 1–22. doi:10.1080/00102202.2019.1646733.

[19] L. D. Lemos, L. A. Q. Llanos, F. M. Pereira, F. R. Centeno, F. H. R. França, Comparison between numerical and experimental data of the radiative heat transfer in a natural gas/CO_2/H_2 turbulent flame, Fuel 281 (2020) 118740. doi:10.1016/j.fuel.2020.118740.

[20] X. Cai, S. Shan, G. Jin, J. Yu, Z. Zhou, New weighted-sum-of-gray-gases radiation model for oxy-fuel combustion simulation of semi-coke from coal-based poly-generation, Thermal Science and Engineering Progress 46 (2023) 102233. doi:https://doi.org/10.1016/j.tsep.2023.102233.

[21] G. Krishnamoorthy, A new weighted-sum-of-gray-gases model for CO_2-H_2O gas mixtures, International Communications in Heat and Mass Transfer 37 (9) (2010) 1182–1186. doi:doi.org/10.1016/j.icheatmasstransfer.2010.07.007.

[22] R. Johansson, B. Leckner, K. Andersson, F. Johnsson, Account for variations in the H_2O to CO_2 molar ratio when modelling gaseous radiative heat transfer with the weighted-sum-of-grey-gases model, Combustion and Flame 158 (5) (2011) 893–901. doi:10.1016/j.combustflame.2011.02.001.

[23] T. Kangwanpongpan, F. H. França, R. C. da Silva, P. S. Schneider, H. J. Krautz, New correlations for the weighted-sum-of-gray-gases model in oxy-fuel conditions based on HITEMP 2010 database, International Journal

of Heat and Mass Transfer 55 (25) (2012) 7419–7433. doi:10.1016/j.ijheatmasstransfer.2012.07.032.

[24] L. J. Dorigon, G. Duciak, R. Brittes, F. Cassol, M. Galarça, F. H. França, WSGG correlations based on HITEMP2010 for computation of thermal radiation in non-isothermal, non-homogeneous H_2O/CO_2 mixtures, International Journal of Heat and Mass Transfer 64 (2013) 863–873. doi:10.1016/j.ijheatmasstransfer.2013.05.010.

[25] M. H. Bordbar, G. Wecel, T. Hyppänen, A line by line based weighted sum of gray gases model for inhomogeneous CO_2-H_2O mixture in oxy-fired combustion, Combustion and Flame 161 (9) (2014) 2435–2445.

[26] F. Cassol, R. Brittes, F. H. França, O. A. Ezekoye, Application of the weighted-sum-of-gray-gases model for media composed of arbitrary concentrations of H_2O, CO_2 and soot, International Journal of Heat and Mass Transfer 79 (2014) 796–806. doi:10.1016/j.ijheatmasstransfer.2014.08.032.

[27] R. Brittes, F. R. Centeno, A. Ziemniczak, F. H. R. França, WSGG model correlations to compute nongray radiation from carbon monoxide in combustion applications, Journal of Heat Transfer 139 (4) (2017) 041202. doi:10.1115/1.4035394.

[28] H. Bordbar, G. C. Fraga, S. Hostikka, An extended weighted-sum-of-gray-gases model to account for all CO_2-H_2O molar fraction ratios in thermal radiation, International Communications in Heat and Mass Transfer 110 (2020) 104400. doi:10.1016/j.icheatmasstransfer.2019.104400.

[29] H. Sadeghi, S. Hostikka, G. C. Fraga, H. Bordbar, Weighted-sum-of-gray-gases models for non-gray thermal radiation of hydrocarbon fuel vapors, CH_4, CO and soot, Fire Safety Journal 125 (2021) 103420. doi:10.1016/j.firesaf.2021.103420.

[30] A. H. B. Selhorst, G. C. Fraga, F. R. Coelho, H. Bordbar, F. H. R. França, A compact WSGG formulation to account for inhomogeneity of H_2O-CO_2 mixtures in combustion systems, Journal of Heat Transfer 144 (7). doi:10.1115/1.4054239.

[31] R. J. C. Fonseca, G. C. Fraga, F. R. Coelho, F. H. R. França, A wide-band based weighted-sum-of-gray-gases model for participating media: Application to H_2O-CO_2 mixtures with or without soot, International Journal of Heat and Mass Transfer 204 (2023) 123839. doi:10.1016/j.ijheatmasstransfer.2022.123839.

[32] J. Consalvi, F. Andre, F. Coelho, F. França, F. Nmira, M. Galtier, V. Solovjov, B. Webb, Assessment of engineering gas radiative property models in high pressure turbulent jet diffusion flames, Journal of Quantitative Spectroscopy and Radiative Transfer 253 (2020) 107169. doi:10.1016/j.jqsrt.2020.107169.

[33] V. Kez, F. Liu, J. Consalvi, J. Ströhle, B. Epple, A comprehensive evaluation of different radiation models in a gas turbine combustor under conditions of oxy-fuel combustion with dry recycle, Journal of Quantitative Spectroscopy and Radiative Transfer 172 (2016) 121–133.

[34] H. Chu, M. Gu, J.-L. Consalvi, F. Liu, H. Zhou, Effects of total pressure on non-grey gas radiation transfer in oxy-fuel combustion using the LBL, SNB, SNBCK, WSGG, and FSCK methods, Journal of Quantitative Spectroscopy and Radiative Transfer 172 (2016) 24–35.

[35] H. Chu, J.-L. Consalvi, M. Gu, F. Liu, Calculations of radiative heat transfer in an axisymmetric jet diffusion flame at elevated pressures using different gas radiation models, Journal of Quantitative Spectroscopy and Radiative Transfer 197 (2017) 12–25. doi:10.1016/j.jqsrt.2017.02.008.

[36] M. Bahador, B. Sunden, Evaluation of weighted sum of grey gases coefficients for combustion gases using predicted emissivities from high resolution

spectroscopic databases, in: Proceedings of ASME Turbo Expo 2008: Power for Land, Sea and Air, ASMEDC, 2008. doi:10.1115/gt2008-51028.

[37] S. Shan, B. Qian, Z. Zhou, Z. Wang, K. Cen, New pressurized WSGG model and the effect of pressure on the radiation heat transfer of H_2O/CO_2 gas mixtures, International Journal of Heat and Mass Transfer 121 (2018) 999–1010. doi:10.1016/j.ijheatmasstransfer.2018.01.079.

[38] C. Paul, S. F. Fernandez, D. C. Haworth, S. Roy, M. F. Modest, A detailed modeling study of radiative heat transfer in a heavy-duty diesel engine, Combustion and Flame 200 (2019) 325–341. doi:10.1016/j.combustflame.2018.11.032.

[39] A. Johnson, S. Zhang, X. Zhao, Wide-band models for high-pressure engine conditions, in: AIAA Propulsion and Energy 2020 Forum, American Institute of Aeronautics and Astronautics, 2020.

[40] J. T. Pearson, B. W. Webb, V. P. Solovjov, J. Ma, Effect of total pressure on the absorption line blackbody distribution function and radiative transfer in H_2O, CO_2, and CO, Journal of Quantitative Spectroscopy and Radiative Transfer 143 (2014) 100–110. doi:10.1016/j.jqsrt.2013.08.011.

[41] J. T. Pearson, B. W. Webb, V. P. Solovjov, J. Ma, Efficient representation of the absorption line blackbody distribution function for H_2O, CO_2, and CO at variable temperature, mole fraction, and total pressure, Journal of Quantitative Spectroscopy and Radiative Transfer 138 (2014) 82–96. doi:10.1016/j.jqsrt.2014.01.019.

[42] J. Cai, M. F. Modest, Improved full-spectrum k-distribution implementation for inhomogeneous media using a narrow-band database, Journal of Quantitative Spectroscopy and Radiative Transfer 141 (2014) 65–72. doi:10.1016/j.jqsrt.2014.02.028.

[43] H. Chu, F. Ren, Y. Feng, M. Gu, S. Zheng, A comprehensive evaluation of the non gray gas thermal radiation using the line-by-line model in one-

and two-dimensional enclosures, Applied Thermal Engineering 124 (2017) 362–370. doi:10.1016/j.applthermaleng.2017.06.037.

[44] Y. Zhou, C. Wang, T. Ren, A machine learning based efficient and compact full-spectrum correlated k-distribution model, Journal of Quantitative Spectroscopy and Radiative Transfer 254 (2020) 107199. doi:10.1016/j.jqsrt.2020.107199.

[45] Y. Liu, J. Zhu, G. Liu, F. Liu, J.-L. Consalvi, Assessment of various full-spectrum correlated k-distribution methods in radiative heat transfer in oxy-fuel sooting flames, International Journal of Thermal Sciences 184 (2023) 107919. doi:10.1016/j.ijthermalsci.2022.107919.

[46] F. R. Centeno, R. Brittes, L. G. Rodrigues, F. R. Coelho, F. H. França, Evaluation of the WSGG model against line-by-line calculation of thermal radiation in a non-gray sooting medium representing an axisymmetric laminar jet flame, International Journal of Heat and Mass Transfer 124 (2018) 475–483. doi:10.1016/j.ijheatmasstransfer.2018.02.040.

[47] K. D. Lathrop, B. G. Carlson, Discrete ordinates angular quadrature of the neutron transport equationdoi:10.2172/4666281.

[48] O. Marin, R. Buckius, A simplified wide band model of the cumulative distribution function for water vapor, International Journal of Heat and Mass Transfer 41 (19) (1998) 2877–2892. doi:10.1016/s0017-9310(98)00033-7.

[49] R. J. C. Fonseca, G. C. Fraga, F. H. R. França, Comparison of the performances of the wide-band based weighted-sum-of-gray-gases and box models in the calculation of non-gray boundaries at high pressures, in: Proceedings of the 27th International Congress of Mechanical Engineering, ABCM, 2023.

5. Appendix A - WBW correlations for the mixture of H_2O and CO_2

Table 5: One gray gas per spectral band and $p = 10\,\text{atm}$.

j	$\kappa_{p,j}$ [$\text{atm}^{-1}\,\text{m}^{-1}$]	$b_{j,0}$	$b_{j,1}$ [K^{-1}]	$b_{j,2}$ [K^{-2}]	$b_{j,3}$ [K^{-3}]	$b_{j,4}$ [K^{-4}]	$b_{j,5}$ [K^{-5}]
				Band 1			
1	41.266	7.854×10^{-1}	3.450×10^{-4}	-2.651×10^{-7}	1.104×10^{-10}	-2.216×10^{-14}	1.542×10^{-18}
				Band 2			
1	16.541	4.041×10^{-1}	2.075×10^{-3}	-2.873×10^{-6}	1.886×10^{-9}	-5.926×10^{-13}	7.180×10^{-17}
				Band 3			
1	4.747	6.441×10^{-1}	1.606×10^{-4}	2.953×10^{-7}	-3.252×10^{-10}	1.206×10^{-13}	-1.572×10^{-17}
				Band 4			
1	1.731	-2.616×10^{-1}	2.023×10^{-3}	-1.720×10^{-6}	8.813×10^{-10}	-2.469×10^{-13}	2.853×10^{-17}
				Band 5			
1	0.664	-2.664×10^{-1}	1.483×10^{-3}	-8.428×10^{-7}	1.764×10^{-10}	8.476×10^{-15}	-5.820×10^{-18}

Table 6: Two gray gases per spectral band and $p = 10\,\text{atm}$.

j	$\kappa_{p,j}$ [$\text{atm}^{-1}\,\text{m}^{-1}$]	$b_{j,0}$	$b_{j,1}$ [K^{-1}]	$b_{j,2}$ [K^{-2}]	$b_{j,3}$ [K^{-3}]	$b_{j,4}$ [K^{-4}]	$b_{j,5}$ [K^{-5}]
				Band 1			
1	6.392	5.901×10^{-2}	2.168×10^{-3}	-3.340×10^{-6}	2.207×10^{-9}	-6.967×10^{-13}	8.536×10^{-17}
2	157.314	7.202×10^{-1}	-1.578×10^{-3}	2.688×10^{-6}	-1.838×10^{-9}	5.923×10^{-13}	-7.370×10^{-17}
				Band 2			
1	4.098	6.541×10^{-1}	-3.377×10^{-4}	-4.406×10^{-9}	1.812×10^{-10}	-9.021×10^{-14}	1.397×10^{-17}
2	92.060	1.598×10^{-1}	6.770×10^{-4}	1.049×10^{-8}	-5.070×10^{-10}	2.902×10^{-13}	-4.916×10^{-17}
				Band 3			
1	0.845	8.045×10^{-1}	-3.996×10^{-4}	2.591×10^{-9}	1.535×10^{-10}	-7.461×10^{-14}	1.122×10^{-17}
2	21.998	-7.505×10^{-2}	6.427×10^{-4}	-2.700×10^{-9}	-2.203×10^{-10}	9.986×10^{-14}	-1.401×10^{-17}
				Band 4			
1	0.363	5.602×10^{-2}	3.526×10^{-4}	-1.083×10^{-9}	-5.686×10^{-11}	1.464×10^{-15}	3.522×10^{-18}
2	3.909	-9.346×10^{-2}	7.268×10^{-4}	5.016×10^{-9}	-4.115×10^{-10}	2.324×10^{-13}	-3.910×10^{-17}
				Band 5			
1	0.228	6.727×10^{-2}	2.462×10^{-4}	-3.665×10^{-10}	9.784×10^{-11}	-8.077×10^{-14}	1.577×10^{-17}
2	2.606	-1.917×10^{-1}	7.385×10^{-4}	8.323×10^{-10}	-4.999×10^{-10}	2.753×10^{-13}	-4.467×10^{-17}

Table 7: Three gray gases per spectral band and $p = 10\,\mathrm{atm}$.

j	$\kappa_{p,j}$ $[\mathrm{atm}^{-1}\,\mathrm{m}^{-1}]$	$b_{j,0}$	$b_{j,1}$ $[\mathrm{K}^{-1}]$	$b_{j,2}$ $[\mathrm{K}^{-2}]$	$b_{j,3}$ $[\mathrm{K}^{-3}]$	$b_{j,4}$ $[\mathrm{K}^{-4}]$	$b_{j,5}$ $[\mathrm{K}^{-5}]$
				Band 1			
1	2.014	4.670×10^{-1}	-9.185×10^{-5}	1.319×10^{-8}	-2.965×10^{-10}	2.052×10^{-13}	-3.818×10^{-17}
2	20.292	-1.696×10^{-1}	5.197×10^{-4}	-1.357×10^{-8}	1.316×10^{-11}	-5.893×10^{-14}	1.571×10^{-17}
3	224.620	5.975×10^{-1}	-2.403×10^{-4}	3.009×10^{-9}	1.272×10^{-10}	-5.424×10^{-14}	6.696×10^{-18}
				Band 2			
1	1.147	6.228×10^{-1}	-6.781×10^{-4}	-7.712×10^{-9}	4.817×10^{-10}	-2.716×10^{-13}	4.521×10^{-17}
2	17.902	-1.525×10^{-1}	1.064×10^{-3}	1.099×10^{-8}	-8.322×10^{-10}	4.869×10^{-13}	-8.262×10^{-17}
3	283.831	3.998×10^{-1}	-1.273×10^{-4}	1.886×10^{-9}	8.779×10^{-11}	-5.184×10^{-14}	8.386×10^{-18}
				Band 3			
1	0.499	4.501×10^{-1}	1.295×10^{-4}	1.026×10^{-8}	-3.750×10^{-10}	2.378×10^{-13}	-4.235×10^{-17}
2	4.182	5.893×10^{-1}	-8.119×10^{-4}	-1.349×10^{-8}	8.691×10^{-10}	-5.170×10^{-13}	8.895×10^{-17}
3	40.812	-2.982×10^{-1}	9.740×10^{-4}	4.459×10^{-9}	-6.283×10^{-10}	3.456×10^{-13}	-5.658×10^{-17}
				Band 4			
1	0.256	2.923×10^{-2}	5.495×10^{-4}	-1.409×10^{-9}	-3.188×10^{-10}	1.464×10^{-13}	-1.951×10^{-17}
2	1.981	6.897×10^{-3}	1.939×10^{-5}	2.546×10^{-9}	2.818×10^{-10}	-1.573×10^{-13}	2.443×10^{-17}
3	7.826	-7.555×10^{-2}	6.006×10^{-4}	2.593×10^{-9}	-5.085×10^{-10}	2.844×10^{-13}	-4.643×10^{-17}
				Band 5			
1	0.156	7.447×10^{-2}	3.432×10^{-4}	7.255×10^{-10}	-5.547×10^{-11}	9.338×10^{-15}	8.150×10^{-19}
2	1.359	-9.669×10^{-2}	2.901×10^{-4}	-1.427×10^{-9}	-5.856×10^{-12}	-1.196×10^{-14}	3.132×10^{-18}
3	6.375	-9.131×10^{-2}	4.255×10^{-4}	1.561×10^{-9}	-3.923×10^{-10}	2.243×10^{-13}	-3.704×10^{-17}

Table 8: Four gray gases per spectral band and $p = 10\,\text{atm}$.

j	$\kappa_{p,j}$ [$\text{atm}^{-1}\,\text{m}^{-1}$]	$b_{j,0}$	$b_{j,1}$ [K^{-1}]	$b_{j,2}$ [K^{-2}]	$b_{j,3}$ [K^{-3}]	$b_{j,4}$ [K^{-4}]	$b_{j,5}$ [K^{-5}]
				Band 1			
1	1.115	8.967×10^{-2}	1.775×10^{-3}	-3.907×10^{-6}	3.099×10^{-9}	-1.083×10^{-12}	1.409×10^{-16}
2	7.801	-1.398×10^{-1}	-1.087×10^{-5}	1.887×10^{-6}	-2.121×10^{-9}	8.476×10^{-13}	-1.179×10^{-16}
3	50.238	4.066×10^{-1}	-8.260×10^{-4}	5.938×10^{-7}	7.842×10^{-11}	-1.270×10^{-13}	2.368×10^{-17}
4	287.062	4.317×10^{-1}	-1.413×10^{-4}	3.175×10^{-7}	-3.273×10^{-10}	1.320×10^{-13}	-1.866×10^{-17}
				Band 2			
1	0.747	1.320	-4.071×10^{-3}	5.269×10^{-6}	-3.290×10^{-9}	9.978×10^{-13}	-1.181×10^{-16}
2	6.831	-1.067	5.025×10^{-3}	-6.677×10^{-6}	4.107×10^{-9}	-1.203×10^{-12}	1.368×10^{-16}
3	40.984	3.252×10^{-1}	-3.695×10^{-4}	6.907×10^{-7}	-3.678×10^{-10}	6.940×10^{-14}	-2.934×10^{-18}
4	447.002	1.060×10^{-1}	6.741×10^{-4}	-1.109×10^{-6}	7.760×10^{-10}	-2.531×10^{-13}	3.135×10^{-17}
				Band 3			
1	0.379	-3.354×10^{-1}	3.071×10^{-3}	-4.630×10^{-6}	3.070×10^{-9}	-9.641×10^{-13}	1.167×10^{-16}
2	2.047	1.289	-3.609×10^{-3}	4.670×10^{-6}	-2.863×10^{-9}	8.486×10^{-13}	-9.773×10^{-17}
3	14.672	3.292×10^{-2}	-3.221×10^{-4}	9.697×10^{-7}	-7.204×10^{-10}	2.462×10^{-13}	-3.228×10^{-17}
4	73.427	-3.460×10^{-1}	1.639×10^{-3}	-1.766×10^{-6}	9.204×10^{-10}	-2.472×10^{-13}	2.695×10^{-17}
				Band 4			
1	0.199	1.876×10^{-1}	-3.719×10^{-4}	1.711×10^{-6}	-1.710×10^{-9}	6.511×10^{-13}	-8.725×10^{-17}
2	1.106	-1.890×10^{-1}	1.387×10^{-3}	-2.684×10^{-6}	2.325×10^{-9}	-8.638×10^{-13}	1.165×10^{-16}
3	3.813	6.175×10^{-2}	-6.448×10^{-4}	2.079×10^{-6}	-1.780×10^{-9}	6.434×10^{-13}	-8.532×10^{-17}
4	14.267	-2.349×10^{-1}	1.462×10^{-3}	-2.129×10^{-6}	1.382×10^{-9}	-4.298×10^{-13}	5.183×10^{-17}
				Band 5			
1	0.126	1.818×10^{-1}	-1.182×10^{-4}	7.569×10^{-7}	-5.984×10^{-10}	1.832×10^{-13}	-1.987×10^{-17}
2	0.915	-2.280×10^{-1}	1.034×10^{-3}	-1.407×10^{-6}	1.014×10^{-9}	-3.341×10^{-13}	4.077×10^{-17}
3	2.921	1.129×10^{-1}	-6.657×10^{-4}	1.707×10^{-6}	-1.427×10^{-9}	4.979×10^{-13}	-6.331×10^{-17}
4	12.553	-2.161×10^{-1}	1.060×10^{-3}	-1.454×10^{-6}	8.836×10^{-10}	-2.535×10^{-13}	2.811×10^{-17}

Table 9: One gray gas per spectral band and $p = 20\,\text{atm}$.

j	$\kappa_{p,j}$ $[\text{atm}^{-1}\,\text{m}^{-1}]$	$b_{j,0}$	$b_{j,1}$ $[\text{K}^{-1}]$	$b_{j,2}$ $[\text{K}^{-2}]$	$b_{j,3}$ $[\text{K}^{-3}]$	$b_{j,4}$ $[\text{K}^{-4}]$	$b_{j,5}$ $[\text{K}^{-5}]$
				Band 1			
1	73.822	1.002	-5.479×10^{-4}	1.114×10^{-6}	-8.714×10^{-10}	3.050×10^{-13}	-3.985×10^{-17}
				Band 2			
1	38.922	2.952×10^{-1}	2.456×10^{-3}	-3.376×10^{-6}	2.222×10^{-9}	-7.038×10^{-13}	8.622×10^{-17}
				Band 3			
1	6.632	6.839×10^{-1}	2.325×10^{-4}	2.184×10^{-7}	-3.291×10^{-10}	1.402×10^{-13}	-2.012×10^{-17}
				Band 4			
1	3.048	-1.815×10^{-1}	1.633×10^{-3}	-9.796×10^{-7}	3.188×10^{-10}	-5.815×10^{-14}	4.999×10^{-18}
				Band 5			
1	0.957	-1.735×10^{-1}	1.157×10^{-3}	-3.362×10^{-7}	-1.421×10^{-10}	1.015×10^{-13}	-1.623×10^{-17}

Table 10: Two gray gases per spectral band and $p = 20\,\text{atm}$.

j	$\kappa_{p,j}$ $[\text{atm}^{-1}\,\text{m}^{-1}]$	$b_{j,0}$	$b_{j,1}$ $[\text{K}^{-1}]$	$b_{j,2}$ $[\text{K}^{-2}]$	$b_{j,3}$ $[\text{K}^{-3}]$	$b_{j,4}$ $[\text{K}^{-4}]$	$b_{j,5}$ $[\text{K}^{-5}]$
				Band 1			
1	8.634	2.545×10^{-1}	1.603×10^{-3}	-2.758×10^{-6}	1.869×10^{-9}	-5.902×10^{-13}	7.165×10^{-17}
2	280.661	7.556×10^{-1}	-1.955×10^{-3}	3.534×10^{-6}	-2.506×10^{-9}	8.199×10^{-13}	-1.022×10^{-16}
				Band 2			
1	6.968	1.012	-1.877×10^{-3}	2.320×10^{-6}	-1.435×10^{-9}	4.401×10^{-13}	-5.266×10^{-17}
2	216.256	-6.075×10^{-1}	4.066×10^{-3}	-5.364×10^{-6}	3.451×10^{-9}	-1.081×10^{-12}	1.313×10^{-16}
				Band 3			
1	1.471	2.030×10^{-2}	2.394×10^{-3}	-3.601×10^{-6}	2.356×10^{-9}	-7.291×10^{-13}	8.725×10^{-17}
2	38.094	6.177×10^{-1}	-1.737×10^{-3}	3.157×10^{-6}	-2.242×10^{-9}	7.298×10^{-13}	-9.043×10^{-17}
				Band 4			
1	0.459	3.043×10^{-1}	-7.953×10^{-4}	2.024×10^{-6}	-1.659×10^{-9}	5.711×10^{-13}	-7.165×10^{-17}
2	6.685	-4.011×10^{-1}	2.161×10^{-3}	-2.439×10^{-6}	1.529×10^{-9}	-4.758×10^{-13}	5.738×10^{-17}
				Band 5			
1	0.264	2.481×10^{-1}	-4.124×10^{-4}	9.903×10^{-7}	-6.056×10^{-10}	1.543×10^{-13}	-1.406×10^{-17}
2	4.131	-3.257×10^{-1}	1.347×10^{-3}	-9.666×10^{-7}	2.646×10^{-10}	-5.653×10^{-15}	-6.105×10^{-18}

Table 11: Three gray gases per spectral band and $p = 20\,\mathrm{atm}$.

j	$\kappa_{p,j}$ $[\mathrm{atm}^{-1}\,\mathrm{m}^{-1}]$	$b_{j,0}$	$b_{j,1}$ $[\mathrm{K}^{-1}]$	$b_{j,2}$ $[\mathrm{K}^{-2}]$	$b_{j,3}$ $[\mathrm{K}^{-3}]$	$b_{j,4}$ $[\mathrm{K}^{-4}]$	$b_{j,5}$ $[\mathrm{K}^{-5}]$
				Band 1			
1	3.100	-3.928×10^{-1}	4.392×10^{-3}	-7.835×10^{-6}	5.747×10^{-9}	-1.926×10^{-12}	2.438×10^{-16}
2	29.327	1.268	-6.301×10^{-3}	1.128×10^{-5}	-8.435×10^{-9}	2.865×10^{-12}	-3.656×10^{-16}
3	372.427	8.544×10^{-2}	1.957×10^{-3}	-3.391×10^{-6}	2.592×10^{-9}	-8.925×10^{-13}	1.147×10^{-16}
				Band 2			
1	1.937	1.328	-3.644×10^{-3}	4.345×10^{-6}	-2.539×10^{-9}	7.312×10^{-13}	-8.301×10^{-17}
2	26.597	-1.162	4.990×10^{-3}	-5.822×10^{-6}	3.299×10^{-9}	-9.175×10^{-13}	1.011×10^{-16}
3	375.122	3.705×10^{-1}	4.399×10^{-4}	-1.088×10^{-6}	9.794×10^{-10}	-3.764×10^{-13}	5.189×10^{-17}
				Band 3			
1	0.718	-5.613×10^{-1}	3.357×10^{-3}	-4.260×10^{-6}	2.428×10^{-9}	-6.684×10^{-13}	7.218×10^{-17}
2	5.355	1.159	-2.431×10^{-3}	2.307×10^{-6}	-9.089×10^{-10}	1.450×10^{-13}	-4.608×10^{-18}
3	69.433	-1.304×10^{-2}	-2.726×10^{-5}	1.231×10^{-6}	-1.264×10^{-9}	4.900×10^{-13}	-6.759×10^{-17}
				Band 4			
1	0.300	3.812×10^{-1}	-1.253×10^{-3}	3.255×10^{-6}	-2.919×10^{-9}	1.076×10^{-12}	-1.426×10^{-16}
2	2.358	-2.019×10^{-1}	1.228×10^{-3}	-2.437×10^{-6}	2.290×10^{-9}	-8.916×10^{-13}	1.234×10^{-16}
3	11.186	-2.251×10^{-1}	1.195×10^{-3}	-7.200×10^{-7}	1.908×10^{-11}	9.303×10^{-14}	-1.982×10^{-17}
				Band 5			
1	0.193	2.612×10^{-1}	-3.730×10^{-4}	1.113×10^{-6}	-8.438×10^{-10}	2.635×10^{-13}	-2.972×10^{-17}
2	1.795	-1.154×10^{-1}	4.219×10^{-4}	-3.999×10^{-7}	3.535×10^{-10}	-1.364×10^{-13}	1.811×10^{-17}
3	9.054	-1.939×10^{-1}	8.593×10^{-4}	-5.451×10^{-7}	2.876×10^{-12}	7.621×10^{-14}	-1.557×10^{-17}

Table 12: Four gray gases per spectral band and $p = 20\,\text{atm}$.

j	$\kappa_{p,j}$ [$\text{atm}^{-1}\,\text{m}^{-1}$]	$b_{j,0}$	$b_{j,1}$ [K^{-1}]	$b_{j,2}$ [K^{-2}]	$b_{j,3}$ [K^{-3}]	$b_{j,4}$ [K^{-4}]	$b_{j,5}$ [K^{-5}]
				Band 1			
1	2.083	-4.887×10^{-1}	4.612×10^{-3}	-8.404×10^{-6}	6.302×10^{-9}	-2.145×10^{-12}	2.743×10^{-16}
2	17.146	1.294	-6.338×10^{-3}	1.175×10^{-5}	-9.132×10^{-9}	3.179×10^{-12}	-4.124×10^{-16}
3	124.311	-2.302×10^{-1}	2.372×10^{-3}	-4.542×10^{-6}	3.790×10^{-9}	-1.374×10^{-12}	1.827×10^{-16}
4	723.996	3.752×10^{-1}	-5.112×10^{-4}	1.071×10^{-6}	-9.195×10^{-10}	3.377×10^{-13}	-4.532×10^{-17}
				Band 2			
1	1.457	1.438	-4.181×10^{-3}	5.005×10^{-6}	-2.905×10^{-9}	8.270×10^{-13}	-9.273×10^{-17}
2	14.456	-1.132	4.609×10^{-3}	-5.380×10^{-6}	2.955×10^{-9}	-7.822×10^{-13}	8.144×10^{-17}
3	89.403	1.231×10^{-1}	8.936×10^{-4}	-1.370×10^{-6}	1.085×10^{-9}	-4.036×10^{-13}	5.550×10^{-17}
4	1171.769	1.406×10^{-1}	3.536×10^{-4}	-6.826×10^{-7}	5.237×10^{-10}	-1.807×10^{-13}	2.315×10^{-17}
				Band 3			
1	0.533	-1.657×10^{-1}	1.241×10^{-3}	-1.082×10^{-6}	2.364×10^{-10}	5.073×10^{-14}	-1.827×10^{-17}
2	2.919	-3.331×10^{-2}	2.397×10^{-3}	-4.465×10^{-6}	3.510×10^{-9}	-1.248×10^{-12}	1.656×10^{-16}
3	20.835	1.523	-5.680×10^{-3}	8.210×10^{-6}	-5.438×10^{-9}	1.731×10^{-12}	-2.128×10^{-16}
4	127.066	-7.164×10^{-1}	2.844×10^{-3}	-3.209×10^{-6}	1.804×10^{-9}	-5.141×10^{-13}	5.836×10^{-17}
				Band 4			
1	0.221	5.365×10^{-1}	-2.164×10^{-3}	4.884×10^{-6}	-4.232×10^{-9}	1.555×10^{-12}	-2.071×10^{-16}
2	1.190	-3.967×10^{-1}	2.422×10^{-3}	-4.397×10^{-6}	3.637×10^{-9}	-1.340×10^{-12}	1.811×10^{-16}
3	5.919	2.498×10^{-1}	-1.426×10^{-3}	3.051×10^{-6}	-2.343×10^{-9}	8.174×10^{-13}	-1.073×10^{-16}
4	21.138	-3.572×10^{-1}	1.974×10^{-3}	-2.693×10^{-6}	1.698×10^{-9}	-5.242×10^{-13}	6.337×10^{-17}
				Band 5			
1	0.156	4.093×10^{-1}	-9.841×10^{-4}	2.062×10^{-6}	-1.524×10^{-9}	4.851×10^{-13}	-5.665×10^{-17}
2	1.015	-3.268×10^{-1}	1.440×10^{-3}	-2.107×10^{-6}	1.544×10^{-9}	-5.154×10^{-13}	6.371×10^{-17}
3	4.149	2.092×10^{-1}	-1.000×10^{-3}	2.105×10^{-6}	-1.614×10^{-9}	5.413×10^{-13}	-6.732×10^{-17}
4	17.376	-2.649×10^{-1}	1.197×10^{-3}	-1.454×10^{-6}	7.904×10^{-10}	-2.056×10^{-13}	2.083×10^{-17}